Chemical Engineering Science 295 (2024) 120133

Contents lists available at ScienceDirect

Chemical Engineering Science

journal homepage: www.elsevier.com/locate/ces

Graphitic carbon nitride nanosheet and ferroelectric $PbTiO_3$ nanoplates S-scheme heterostructure for enhancing hydrogen production and textile dye degradation

Rashmiranjan Patra [a], Pradeep Kumar Panda [a], Ting-Han Lin [b], Ming-Chung Wu [b], Po-Chih Yang [a,*]

[a] Department of Chemical Engineering and Materials Science, Yuan Ze University, Taoyuan 32003, Taiwan
[b] Department of Chemical and Materials Engineering, Chang Gung University, Taoyuan 33302, Taiwan

ARTICLE INFO

Keywords:
$g\text{-}C_3N_4$
$PbTiO_3$
Photocatalysis
Hydrogen production
S-scheme heterojunction
Dye degradation

ABSTRACT

Graphitic carbon nitride ($g\text{-}C_3N_4$) is a reliable photocatalyst that can be activated by visible light. However, its photocatalytic efficiencies are hindered by the rapid recombination of charge carriers on its surface. A hybrid photocatalyst consisting of a ferroelectric $PbTiO_3$ nanoplate/$g\text{-}C_3N_4$ S-scheme heterojunction was synthesized using an ultrasonic-assisted hydrothermal method, to overcome the aforementioned limitation. The $PbTiO_3$ nanoplates incorporated into the $g\text{-}C_3N_4$ matrix created a strong electric field, resulting in superior photocatalytic activities. This improvement can be attributed to the efficient separation of the photogenerated charge carriers. The hybrid photocatalyst (10PTCN) exhibits an impressive H_2 evolution rate (1587.82 $\mu mol.g^{-1}.h^{-1}$) under simulated solar irradiation. The hybrid photocatalysts demonstrated 99.40 % methylene blue (30 $mg{\cdot}L^{-1}$) in 90 min under simulated solar irradiation with remarkable reusability. This work contributes to enhancing the understanding of utilizing ferroelectric 2D nanoplates to develop efficient charge transfer schemes for improved photocatalysts.

1. Introduction

The sudden increase in global population not only caused a severe food shortage but also led to an energy crisis due to the overconsumption of fossil fuels. The energy crisis is a long-term concern that continues to grow alongside advancements in science and technology. Scientists and government agencies are working to find a reliable and cost-effective way to replace renewable energy with alternative fossil fuels. Solar energy is widely accessible as a renewable energy source (Şen, 2004). The solar energy that reaches the earth's surface at any given moment is equivalent to the output of a 130 million 500 MW power plant, making it an abundant and inexhaustible energy source (Li and Li, 2017). Preserving solar energy as hydrogen energy may help mitigate the consequences of global climate change and excessive fossil fuel usage (Hassan et al., 2023; Megía et al., 2021; Osman et al., 2022).

Water splitting using semiconductor photocatalysts has garnered significant attention as a method for green hydrogen production. This is primarily due to its ease of implementation, efficiency, and affordability (Hisatomi and Domen, 2019; Hisatomi et al., 2014). Out of these, metal-free graphitic carbon nitride ($g\text{-}C_3N_4$) stands out due to its facile synthesis process, high surface area, good thermal and chemical stability, and low preparation cost (Ong et al., 2016). It exhibits a moderate band gap of 2.7 eV, which can effectively absorb visible light (50 % of the total solar spectrum) (Ji et al., 2017). Despite these notable characteristics, pure $g\text{-}C_3N_4$ (CN) exhibits negligible photocatalytic activity because of fast carrier recombination at its surface (Dash et al., 2024). The absorption of photons, isolation of charge carriers (electrons and holes), and surface reaction with external species are the three main aspects that control the photocatalytic efficiency of any material (Xu et al., 2021).

Various strategies have been proposed periodically to separate the charge carriers generated by light and enhance their longevity (Bai et al., 2022; Hu et al., 2021; Nasir et al., 2019; Ong et al., 2016). Among them, creating an effective internal electric field has received much attention. The internal electric field can separate the photogenerated charge carriers, allowing for efficient photocatalytic activity (Liu et al., 2023). Constructing heterojunctions by combining a variety of semiconductors is an effective method for accomplishing this goal. However, in most

* Corresponding author.
E-mail address: pcyang@saturn.yzu.edu.tw (P.-C. Yang).

https://doi.org/10.1016/j.ces.2024.120133
Received 6 January 2024; Received in revised form 9 April 2024; Accepted 15 April 2024
Available online 16 April 2024

cases, this in-built electric field is present close to the interface of the hybrid photocatalysts, which further limits the ability to improve catalytic effectiveness (Chen et al., 2023; Xie et al., 2022). In contrast, the electric field induced by ferroelectric polarisation has recently been in the limelight because of its efficacy in preventing charge carrier recombination. Ferroelectric materials exhibit spontaneous dipole moments in the absence of applied stress. These moments generate spontaneous polarization, enabling the isolation and migration of charge carriers from the bulk to the surface. (Chen et al., 2019; Li et al., 2020; Lv et al., 2022). Perovskite-type materials, such as $BaTiO_3$, $PbTiO_3$, $SrTiO_3$, $BiFeO_3$, etc. are commonly used in photocatalytic applications among the various ferroelectric materials (Patra et al., 2023a). Nevertheless, materials such as $BaTiO_3$ and $SrTiO_3$ have a poor light absorption ability due to a broad band gap (greater than 3 eV). As a result, they can only utilize ultraviolet (UV) light (~5 % of total solar energy) (Elmahgary et al., 2023; Kuang and Yang, 2013), while for $BiFeO_3$, it is difficult to control the ferroelectric polarization in nanoparticles (Liu and Huang, 2022).

However, $PbTiO_3$ (PT) is a photocatalyst activated by visible light with a relatively small bandgap (Kooshki et al., 2019). It possesses a non-centrosymmetric structure (Qin et al., 2023) and exhibits both ferroelectric and piezoelectric properties, which are quite beneficial for photocatalytic activity (Feng et al., 2020). Regardless of these remarkable qualities, a solid Schottky barrier prevents its application in photocatalytic hydrogen production (Liu et al., 2018). Due to the contrasting work functions, this barrier develops near the interface between the ferroelectrics and co-catalysts like Pt, Au, etc. (Zhang and Yates, 2012). To overcome these obstacles and create an efficient visible light photocatalyst, ferroelectric PT can be coupled with CN to form a hybrid heterostructure catalyst. Xu et al. demonstrated, for the first time, that the photocatalytic H_2 evolution rate can be increased by combining CN and PT (PTCN) with polyhedron morphology fabricated using a high-temperature method, compared to pristine CN and PT (Xu et al., 2021). In comparison to other morphologies like nanospheres or nanocubes, one- and two-dimensional ferroelectric nanomaterials, such as nanoplates and nanowires, generally have a higher bending tolerance and flexibility. They are more efficient at producing polarized charges from mechanical stress (Xie et al., 2022). Huang et al. fabricated PT/CdS composite, which enhanced piezo-photocatalytic H_2 production (Huang et al., 2021). Xie et al. constructed a NiO@PT p-n junction, where the ferroelectric polarization from PT nanoplates, along with the piezoelectric effect showed a greater photocatalytic RhB degradation rate ($k = 0.46\ min^{-1}$) (Xie et al., 2022). However, as far as we know, the exploration of heterostructures consisting of PT nanoplates with CN, and their hydrogen production or dye degradation performance, has not yet been undertaken. Among these, the remarkable achievement is the creation of a novel heterojunction with an S-scheme that incorporates photocatalysts for both reduction and oxidation (Meng et al., 2021; Wang et al., 2023). Researchers have been drawn to it because of its improved redox capacity and efficient isolation of photoinduced charge carriers. The charge migration in an S-scheme heterojunction is primarily affected by the internal electric field and band bending near the interface (Lu et al., 2023; Xu et al., 2022). The S-scheme heterojunction outperforms single catalysts and regular type-II heterojunctions by greatly extending the photon absorption range and enhancing the electron migration rate at the interface (Xu et al., 2019; Zhang et al., 2022). To improve the photocatalytic efficiency, it is crucial to choose a suitable semiconductor for constructing an S-scheme heterojunction with PT (Qin et al., 2023). Due to the appropriate matching of their band configurations, an S-scheme heterojunction can be developed between CN and the perovskite-based metal titanate (Alam et al., 2023; Huang et al., 2022; Li et al., 2024; Li et al., 2022), which will result in exceptional redox ability and effective charge separation.

Herein, we synthesized innovative S-scheme heterojunction hybrid composites based on 2D PT nanoplates and CN nanosheets via an ultrasonic-assisted hydrothermal method. The hybrid composites' chemical composition, structural, morphological, and optical properties were studied in detail. The photocatalytic applications were studied for hydrogen production from water splitting under simulated solar irradiation and degradation of organic textile dyes such as Methylene Blue (MB) and Rhodamine B (RhB) under low-cost domestic halogen lamps. Further, the photocatalytic mechanism is investigated using the active species trapping test, which suggests a possible S-scheme charge transfer mechanism. This study provides an insightful discussion on the concept of using ferroelectricity to develop next-generation photocatalysts for environmental remediation and green energy production.

2. Materials and methods

2.1. Materials

Lead nitrate [$Pb(NO_3)_2$], Titanium dioxide (TiO_2), RhB, and ethylenediaminetetracetic acid disodium (EDTA-2Na) were purchased from Sigma Aldrich (Shanghai, China). Polyethylene glycol (PEG, Mw: 20000), $PtCl_4$ (99.9 %) and 1,4-benzoquinone (98+%) were supplied by Thermo Scientific, UK. Hydrogen peroxide (H_2O_2, 30 %) was purchased from SHOWA, Japan. Tert-Butyl alcohol and nitric acid (HNO_3, 70 %) was obtained from J.T. Baker, USA. Silver nitrate ($AgNO_3$) was provided by Fisher Scientific, UK. Potassium hydroxide (KOH) was purchased from Honeywell, Fluka, France. UniRegion Biotech, Taiwan supplied Urea (CH_4N_2O, 99 %). MB (95 %) was obtained from Combi-Blocks, USA, and ethanol was purchased from ECHO Chemical Co. Ltd., Taiwan. All the chemicals and reagents were analytical grade and used without additional processing.

2.2. Synthesis of g-C_3N_4

g-C_3N_4 was synthesized following our earlier research (Patra et al., 2023b). Urea was treated at 250 °C for 1 h, 350 °C for 2 h and 550 °C for 2 h, respectively in a muffle furnace, and cooled to ambient temperature. The resultant yellow powder was labelled CN, ground in a mortar, and stored for further use.

2.3. Synthesis of PT

PT was synthesized using a hydrothermal method. First, 12.36 g of KOH was dispersed into 20 mL of deionized (DI) water to prepare the 11 mol KOH solution. Next, TiO_2 (0.6 g) was dissolved into the KOH solution using a magnetic stir bar for 0.5 h to obtain a homogenous solution. Meanwhile, $Pb(NO_3)_2$ solution was prepared by dispersing 3.23 g Pb $(NO_3)_2$ in 10 mL of DI water and stirring with a magnetic stir bar until a clear solution was obtained. Subsequently, the Pb precursor solution was carefully added dropwise to the Ti precursor solution. The solution turned light pink in colour and was kept on stirring for 20 mins. Finally, 10 mL of DI water and 10 mL of PEG solution (1 g. L^{-1}) were added followed by stirring for 3 h. This suspension was transferred into a 100 mL stainless steel autoclave with a teflon lining and heated to 200 °C for 10 h. Following the completion of the reaction, the autoclave was consequently cooled to ambient temperature. The sample was collected from an autoclave by centrifugation and washed with 1 % nitric acid, ethyl alcohol, and DI water, respectively, repeatedly and then dried at 80 °C overnight. The pale-yellow PT powder was finally obtained by annealing the obtained powder for 1 h at 430 °C, (Xie et al., 2022) and then cooling it to room temperature.

2.4. Synthesis of PTCN heterojunction

PTCN heterojunction was constructed via an ultrasonic-assisted hydrothermal method. In detail, 500 mg of CN and a certain amount of PT were dissolved in ethyl alcohol separately and kept for the ultrasonic treatment for 1 h to make the homogenous dispersion. Both solutions were mixed under nitrogen atmosphere (99.98 % purity), and treated

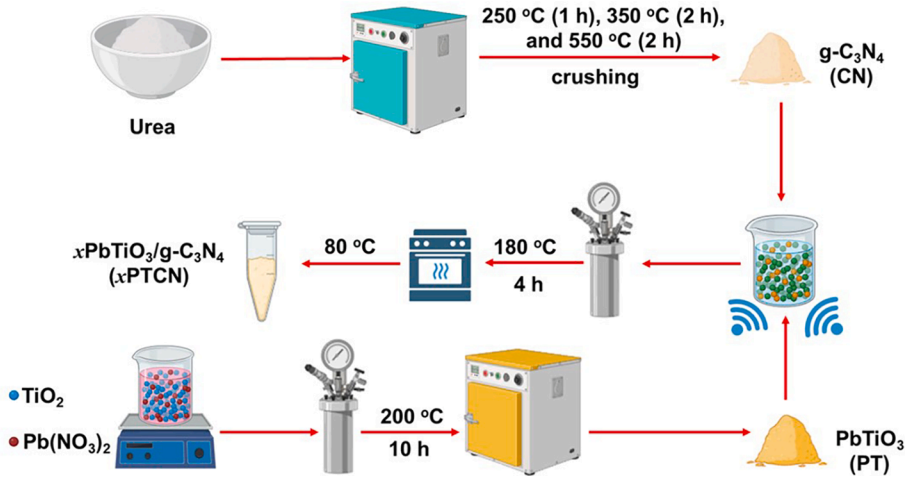

Scheme 1. Schematic illustration of catalyst preparation.

ultrasonically for 1 h. The suspension was then sealed for 4 h at 180 °C in a 50 mL teflon-lined stainless-steel autoclave. The obtained precipitate was washed with DI water and ethanol repeatably and dried at 80 °C overnight to obtain the final product. Similarly, 5PTCN, 7PTCN, 10PTCN, and 15PTCN were prepared with varying the amount of PT to 5 wt%, 7 wt%, 10 wt%, and 15 wt% respectively in the CN matrix.

2.5. Characterization

The morphology of the composites was examined by employing field emission scanning electron microscopy (FE-SEM) (JSM-6701F, JEOL, Tokyo, Japan). The morphology of the samples was inspected by employing transmission electron microscopy (TEM) (JEOL JEM-F200) at a voltage of 200 kV. The phase and crystal structure of the prepared samples were determined using X-ray diffraction (XRD) (X′ pert 3Powder, Malvern, PANalytical, Netherlands). X-ray photoelectron spectroscopy (XPS) analysis (Al K-Alpha from Thermo Fisher Scientific Inc. in East Grinstead, UK) determined the binding energy and surface chemical composition. Brunauer-Emmett-Teller (BET) method (ASAP2020, Micromeritics, Norcross, GA, USA) was used to calculate the specific surface area (SSA), with N_2 acting as an adsorber. To identify the surface functional groups of the samples, Fourier transform infrared (FTIR) spectroscopy (Perkin Elmer, Llantrisant) was used, with KBr serving as the background, and measurements made between 4000 and 500 cm^{-1}. Thermal stability was measured in an oxygen-rich atmosphere at 800 °C with a ramp of 10 °C min^{-1} using a thermogravimetric analyzer (Q50, TA, New Castle, DE, USA). The optical absorbance spectra of the composites were examined using a diffuse reflectance spectroscopy (DRS) spectrometer (JASCO 670). The photoluminescence (PL) emission spectra of sample suspensions were analysed using a fluorescence spectrometer (Hitachi F-7000 FLS920P) at an excitation of 365 nm.

2.6. Photocatalytic hydrogen production

The 300 mL glass reactor under 300 W Xenon illumination (Perfectlight PLS-SXE300) was used in the photocatalytic hydrogen production experiment. The system was operated in the Labsolar 6A system (Perfectlight Technology, Beijing, China) without using an optical filter and with continuous stirring using a magnetic stir bar. The light source's distance from the solution's was kept around 6 cm. A certain amount of catalyst (50 mg) was evenly distributed throughout 100 mL of an equal volume mixture containing ethanol and DI water. $PtCl_4$ aq. solution (2 wt%) was added to the above solution by sonication for 10 min. The reaction temperature was kept around 25 °C to 28 °C by flowing the cold water using a thermostat. Using Helium as a carrier gas and an online gas chromatography system along with a barrier ionization discharge detector (Shimadzu, Nexis GC-2030, Kyoto, Japan), the concentration of hydrogen was measured every 1 h over 3 h.

2.7. Photocatalytic dye degradation

For the photocatalytic degradation, MB solution (30 mg L^{-1}) was chosen as the target pollutant. A domestic halogen lamp (100 W) was used as light source. The lamp was illuminated 30 mins before the experiment to stabilize the output intensity. The synthesized photocatalyst (50 mg) was dissolved in 50 mL of MB solution and stirred under the dark at ambient temperature to achieve the adsorption–desorption equilibrium. Prior to the light exposure, 30 μL of H_2O_2 was added to the photocatalyst dye solution. The lamp was maintained at a distance of 6 cm from the dye solution containing photocatalyst. Cold water from a thermostat was circulated throughout the experiment to keep the reactor temperature constant at (25 ± 0.5) °C. The whole system was set up inside a dark box to prevent the light energy loss. 3 mL of reaction solution was taken out at the same interval and centrifuged at 12,500 rpm for 20 min to separate the photocatalyst through filtration by using 0.22 μm PVDF filter. The residue MB concentration was measured by using a UV–vis spectrometer by considering the characteristic maximum peak of MB at 664 nm. The degradation efficiency (η) can be calculated by using Lambert-Beer law,

$$\eta = \frac{A_i - A_t}{A_i} \times 100\% = \frac{C_i - C_t}{C_i} \times 100\% \quad (1)$$

Where, 'A_i', and 'C_i' are the absorbance and concentration of initial MB solution and A_t and C_t are the absorbance and concentration of MB solution at time t (min), respectively.

Further, the pseudo-first order kinetic model was employed to study the MB degradation. The rate constant was calculated by using the following equation,

$$-\ln\left(\frac{C_t}{C_0}\right) = kt \quad (2)$$

Where, C_0 is the MB concentration at adsorption–desorption equilibrium, k is the reaction rate constant, and t is the irradiation time.

The photodegradation of RhB was performed under the similar conditions as MB photodegradation by replacing MB by RhB solution (10 mg. L^{-1}) and observing the characteristic peak at 554 nm.

To investigate the influence of reactive oxygen species (ROS), active species trapping experiment was conducted. 10 mM of Ethylenediaminetetraacetic acid (EDTA-2Na), 1,4-Benzoquinone, *tert*-butyl alcohol (t-BuOH) and $AgNO_3$ were chosen as scavengers to capture holes

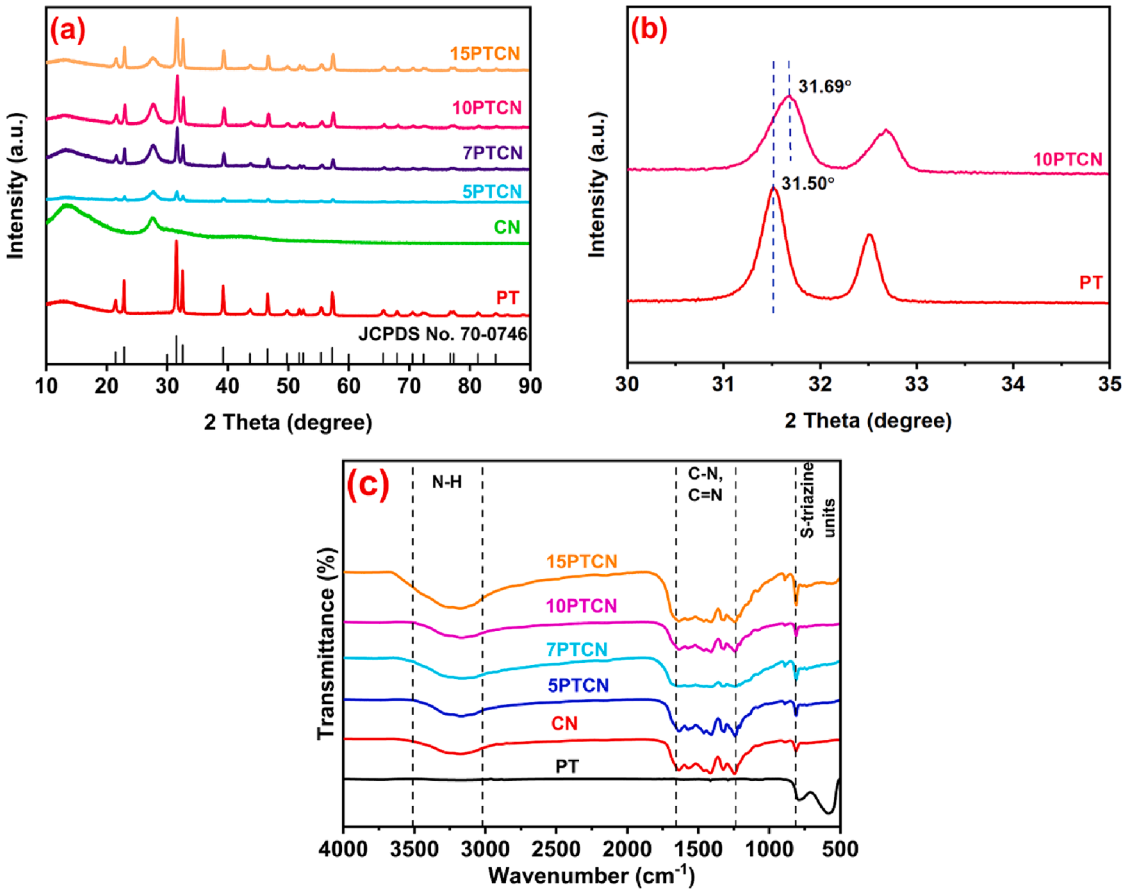

Fig. 1. (a) The XRD patterns, (b) magnified image of XRD patterns, and (c) FTIR spectra of PT, CN, and PTCN samples.

(h^+), superoxide radicals ($\bullet O_2^-$), hydroxyl radicals (•OH) and electrons (e^-) respectively. 1 mL of each scavenger was added to the dye solution containing H_2O_2 and photocatalysts. The overview of catalyst preparation is provided in Scheme 1.

3. Results and discussion

3.1. Structural analysis

X-ray diffraction (XRD) patterns of CN, PT, and PTCN heterojunction structures were analyzed to validate the formation of heterojunction, identify phases, and comprehend crystal structure. From Fig. 1a, two main peaks of CN were observed at 13.1° and 27.5° which is consistent with the weak intra-layer diffraction of the (1 0 0) plane and inter-planner graphite stacking of (2 0 0) plane (JCPDS no. 87-1526), respectively (Patra et al., 2023b). Furthermore, all diffraction peaks for PT are well matched with the tetragonal PT phase (JCPDS no. 70-0746) (Chao et al., 2012). From Fig. 1a, all the diffraction peaks of PT and CN can be spotted in PTCN heterojunctions without any additional peaks, which confirmed hybrid photocatalyst has no impurity. The (1 0 1) peak at 31.5° of PT is very sharp and with an increase in PT content this (1 0 1) peak gets more sharper in the composite while the peak corresponds to CN at 27.5° gradually weakened which further confirms the presence of both PT and CN in the composite materials. To achieve the effective movement of charge carriers through the heterostructure, the components must be closely intact with each other. In 10PTCN sample, the (1 0 1) lattice plane of PT slightly shifted from 31.50° to 36.69° (Fig. 1b). This reflects the successful creation of PTCN heterojunction near the interface between CN and PT (Zhu et al., 2022). To better understand how PT and CN are linked together in the heterostructure, Further Fourier transform infrared (FTIR) spectra were acquired. A broad peak was observed at 3000 – 3500 cm^{-1} in CN (Fig. 1c) can be associated with N-H, meanwhile, the peaks at 1240–1640 cm^{-1} correspond to C–N and C = N (Bao et al., 2022). The bending vibration of triazine units is responsible for the sharp peak at 804 cm^{-1}. The peak at approximately 585 cm^{-1} in the PT spectrum is attributed to the Ti-O (Xu et al., 2021). In the 10PTCN sample, all the stretching modes of CN are present while a moderate stretching of Ti-O at 585 cm^{-1} can be observed. The weakened Ti-O peak may be attributed to a small amount of PT in the heterostructure (Xu et al., 2021).

3.2. Morphological analysis

The morphology of photocatalysts was investigated by field emission scanning electron microscopy (FE-SEM). Fig. 2a displays the FE-SEM image of hydrothermally prepared PT nanoplates with a rectangular outline and smooth surface. Fig. 2b shows the lamellar 2D layered structure of CN as reported in previous literature (Wang et al., 2020; Xu et al., 2021) with the notable exposed surface, which will provide more favourable sites for the reaction to take place. From Fig. 2c, it can be observed that the PT nanoplates are evenly distributed in the CN matrix. From the transmission electron microscopy (TEM) images as well as from DLS (dynamic light scattering) (Fig. S1a and c) it was found that the size of the PT nanoplates ranges in between 200−500 nm. According to previous literature, when the size of the PT nanoplates decreases below 200 nm, the size-dependent ferroelectricity decreases rapidly (Xu et al., 2021). As the particle size increases along the polarization direction, the ability of PT nanoplates to separate charges increases as well because of the growing potential difference between the opposing polarization facets. Moreover, the acceleration of the photocatalytic hydrogen evolution reaction activity in ferroelectric materials is directly attributed to this driving force for charge separation (Liu et al., 2020). It

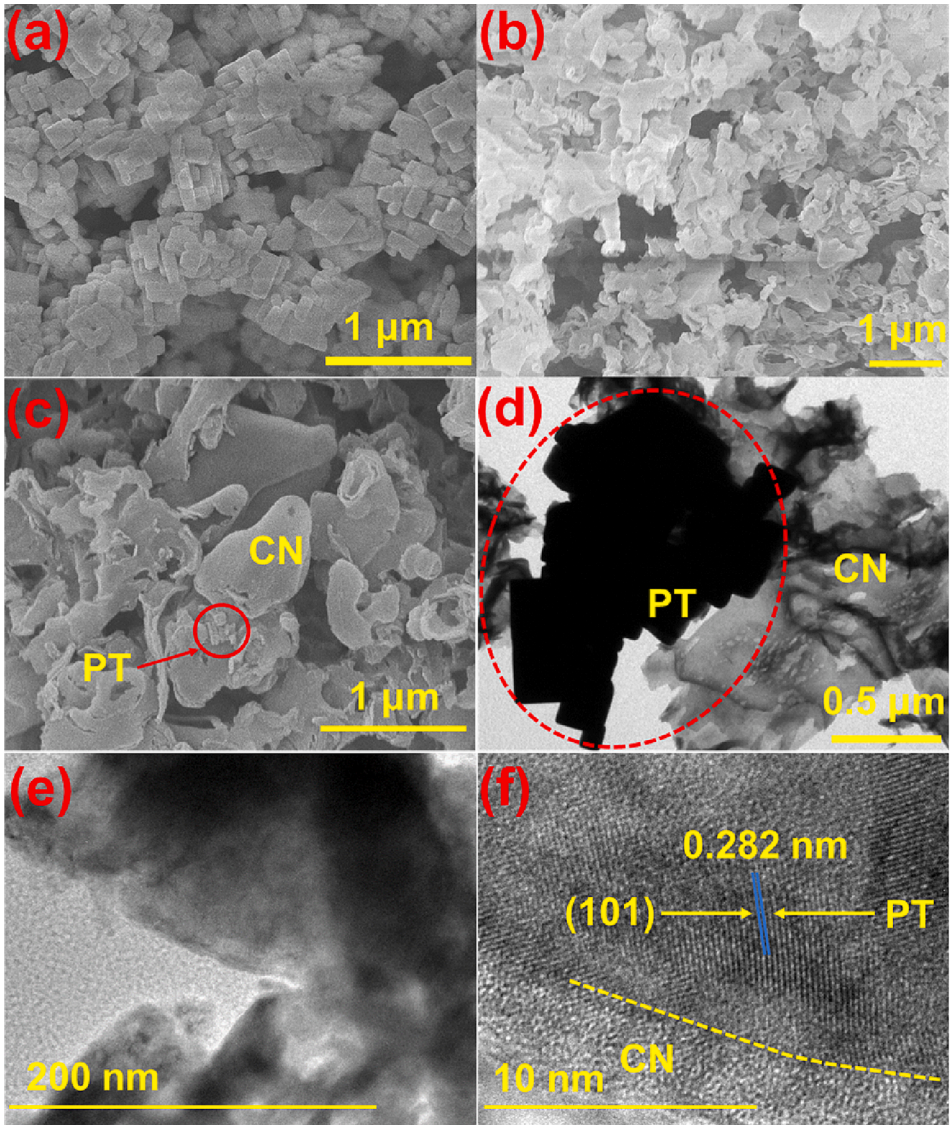

Fig. 2. FE-SEM images of (a) PT, (b) CN, (c) 10PTCN, (d) TEM, and (e) HR-TEM image of 10PTCN, and (f) corresponding interface between PT and CN.

has also been observed that for large-sized PT nanoplates (700 – 800 nm and above) the photocatalytic effect is considerably weaker because of longer migration distance of charge carriers and reduction in active sites which comes along with the increase in particle size (Xie et al., 2022). Based on these findings, the size of the PT nanoplates prepared in this work is favourable for photocatalytic application. The HR-TEM image of CN in Fig. S1b reveals the 2D nanosheet structure of CN in the 10PTCN hybrid structure. From Fig. 2d strong interaction between PT nanoplates and CN nanosheets can be spotted. From the High-resolution TEM images (Fig. 2e and f) of 10PTCN, clear lattice fringes of PT can be observed, which confirms its crystalline nature. The presence of a distinct interface between CN and crystalline PT nanoplates ensures the formation of a hybrid structure by the ultrasonic-assisted hydrothermal approach.

3.3. Surface element analysis

The XPS spectrums of PT, CN, and 10PTCN are shown in Fig. 3a. The spectra of PT and CN show the presence of their respective elements with pure phases without any impurity. For the 10PTCN sample, elements from both the PT and CN are present which confirms the successful addition of PT nanoplates into 2D CN sheets. From Pb 4f spectrum in Fig. 3b. two distinctive peaks of Pb^{2+} can be observed at 137.65 eV for $4f_{7/2}$ and 142.5 eV for $4f_{5/2}$, which corresponds to Pb-O. Meanwhile, for 10PTCN, these two peaks shifted towards low binding energies to 137.45 eV and 142.17 eV for $4f_{7/2}$ and $4f_{5/2}$, respectively which confirms the electronic interaction between PT and CN. In addition to that, two additional peaks at 138.32 eV and 142.65 eV were detected for 10PTCN which may be attributed to the origination of Pb-NO_2 (Xu et al., 2021). In Fig. 3c, the high-resolution Ti 2p is deconvoluted into four major parts. The presence of Ti $2p_{3/2}$ and Ti $2p_{1/2}$ at 458.3 eV and 464.13 eV respectively confirms the presence of Ti^{4+} while the appearance of Ti $2p_{3/2}$ at 457.53 eV and Ti $2p_{1/2}$ at 463 eV confirms the presence of Ti^{3+} state in PT. The presence of Ti^{3+} state is caused by the oxygen vacancy-related defects which control the dielectric properties of the materials. Furthermore, low valance Ti^{3+} was found to be effective in restricting the recombination of photogenerated charge carriers and thus, promoting the charge separation (Paramanika et al., 2018). For 10PTCN heterostructure both of these Ti^{3+} and Ti^{4+} are present. Fig. 3d. depicts the O 1s spectrums of PT and 10PTCN. The peak at 529.09 eV represents the oxygen in PT lattice (Ti-O) whereas the peak at 530.09 eV represents the surface absorbed hydroxyl groups (–OH) of PT (Huang et al., 2021). For 10PTCN, two additional peaks in 10PTCN appeared at 532.47 eV and 533.8 eV which can be due to the presence of

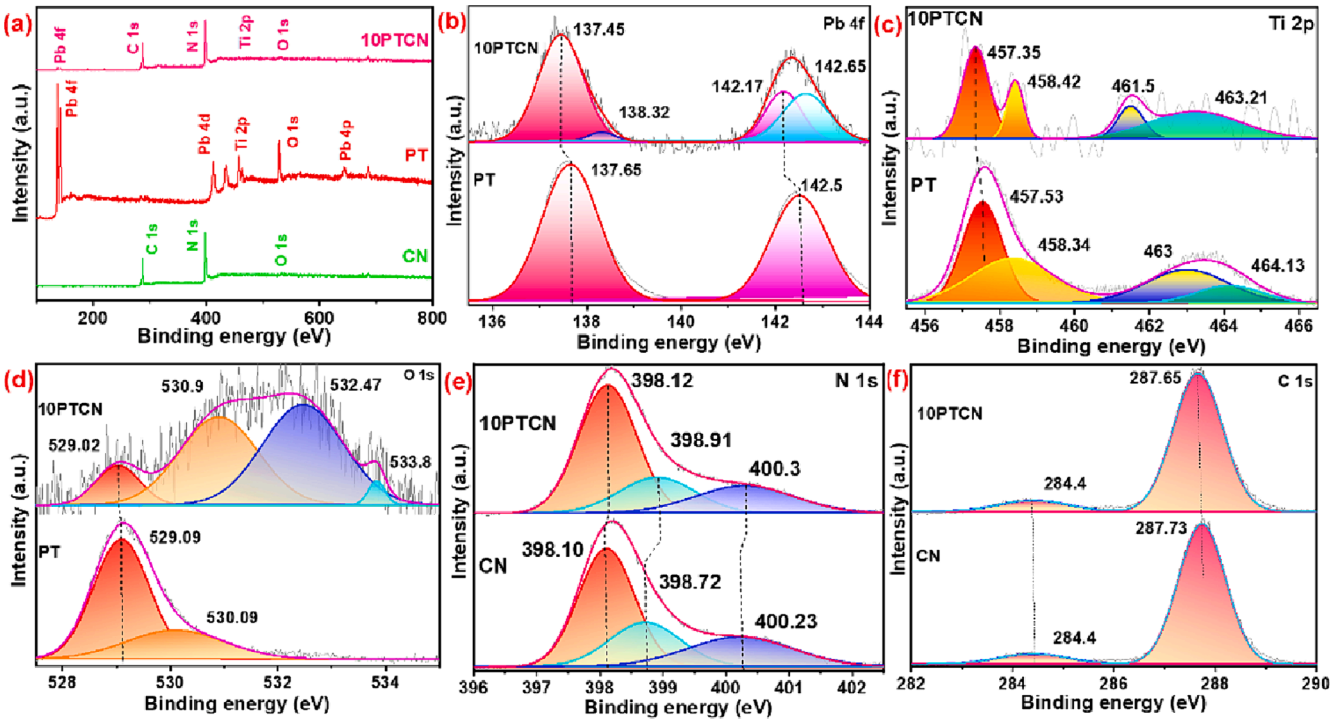

Fig. 3. (a) XPS spectra of PT, CN, and 10PTCN, and high resolution XPS spectra of (b) Pb 4f, (c) Ti 2p, (d) O 1s of PT and 10PTCN, (e) N 1s, and (f) C 1s of CN, and 10PTCN.

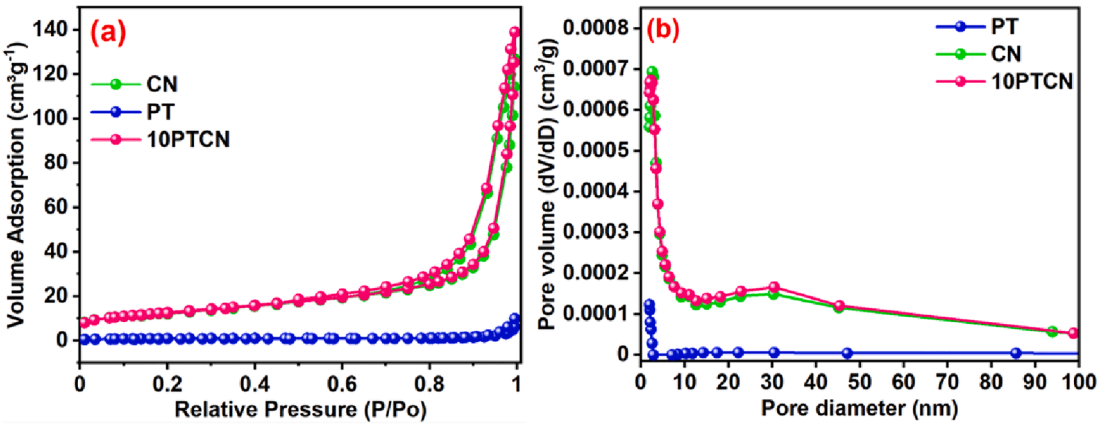

Fig. 4. (a) BET isotherms, and (b) pore size distribution of PT, CN, and 10PTCN.

C-O and O = C-O respectively (Xing et al., 2016), which further confirms the interaction between the PT and CN. The N 1s peak of CN (Fig. 3e) consists of three peaks corresponding to C-N = C at 398.1 eV, N-$(C)_3$ at 398.72 eV, and C-N-H at 400.23 eV (Xu et al., 2021). Nevertheless, the interaction between CN and PT shifts all of these three characteristic peaks towards the higher binding energy peaks at 398.12 eV, 398.91 eV, and 400.3 eV, respectively. Fig. 3f verifies that the C 1s peak of CN can be attributed to a couple of peaks at 284.4 eV and 287.73 eV. The former peak represents the C-C/adventitious carbon bonds while the latter is associated with N-C = N in aromatic groups (Adhikari et al., 2017).

The binding energy (BE) of the constituent elements usually decrease when they gain electrons and increase when they lose electrons. This binding energy change phenomena reflected a robust interaction between the two constituents at their interfaces. As a result of the Pb and N multivalence results (Fig. 3b and e), electrons flow from CN to PT and reach thermodynamic equilibrium (Bao et al., 2022). These results clearly showed that PT and CN were tightly coupled resulting in PTCN heterojunctions, which are favourable for the photocatalysis due to significant movement of charge carriers through the interface between both elements of the heterojunction.

3.4. Surface area and pore structure analysis

Physical factors such as surface area and textural morphology impact the behavior and interactions of solid materials (Oluwole and Olatunji, 2023). The physical microstructure, textural characteristics, surface area, and pore structure of the photocatalysts were studied through the N_2 adsorption–desorption studies. The Brunauer-Emmett-Tellar (BET) isotherms in Fig. 4a for PT, CN, and 10PTCN shows a type IV characteristic, which reflects the existence of mesopores (2−50 nm) with a H3 class of hysteresis loop. According to previous studies, H3 hysteresis comes from plate-like layered structure aggregation (Thommes et al., 2015), establishing slit-like pores (Oluwole and Olatunji, 2023) which is consistent with our SEM and TEM data (section 3.2). The specific surface

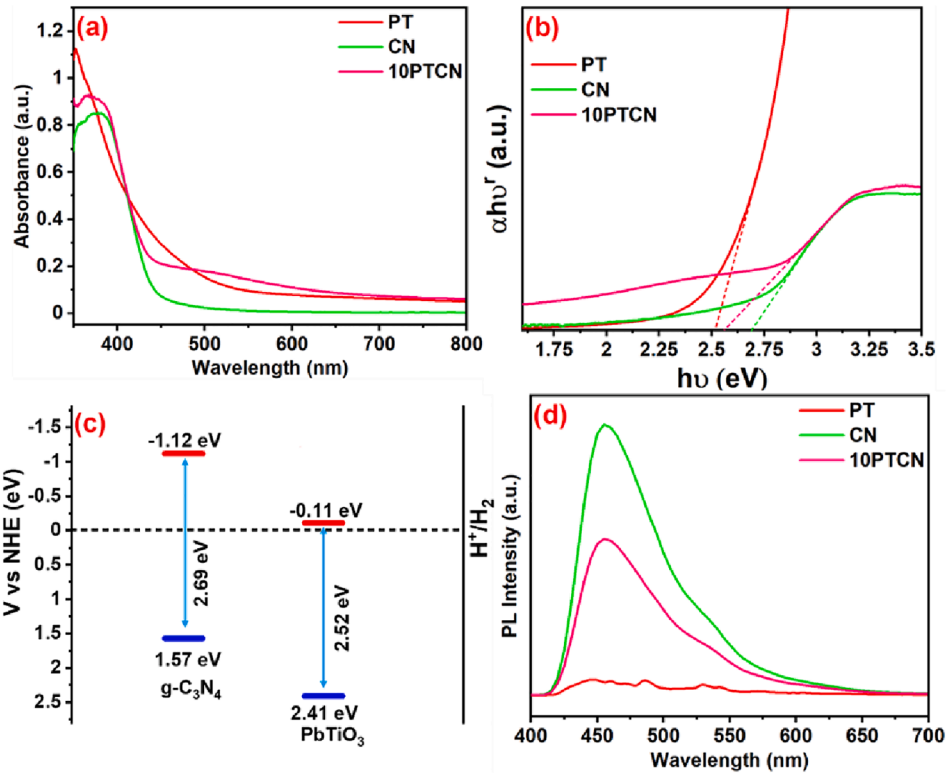

Fig. 5. (a) UV–vis DRS absorption spectra, and (b) the Tauc's plot of PT, CN, and 10PTCN, (c) band structure alignment of PT and CN, (d) PL spectra of PT, CN, and 10PTCN.

area (SSA) for PT, CN, and 10PTCN are found to be 3.2966 $m^2.g^{-1}$, 43.5448 $m^2.g^{-1}$, and 44.2227 $m^2.g^{-1}$, respectively (Table S1). Notably, after the introduction of PT into the CN sheets, the SSA of the 10PTCN heterostructure increased marginally compared to that of PT and CN. Moreover, the SSA of 10PTCN contains 86.5 % of mesopores while the CN contains 82.5 % of mesopores. This increased SSA as well as pore volume in the 10PTCN is beneficial for the adsorptions of pollutants and supplies additional active sites for photocatalytic activity, boosts electron transfer kinetics and infusibility/diffusibility of intraparticles (Gong et al., 2023; Oluwole and Olatunji, 2023). Previously, Xu et al. revealed that the PTCN heterojunction made from a thermal treatment (Xu et al., 2021) possessed an SSA of 26.2 $m^2.g^{-1}$, while in this work, the PTCN heterojunction made from an ultrasonic-assisted hydrothermal method exhibits a SSA of 44.2 $m^2.g^{-1}$, which is 1.6 times higher, indicating an improved photocatalytic activity.

3.5. Optical properties analysis

A semiconductor's optical absorption is known to be closely related to its electronic structure. The optical characteristics of heterojunction photocatalysts were studied using UV–Vis spectra. Fig. 5a shows the optical absorption spectra of CN, PT, and 10PTCN. Both CN and PT have absorption edges positioned between 400−500 nm, indicating that they can utilize the visible light spectrum. The absorption edge of the 10PTCN photocatalyst is positioned between the PT and the CN. The energy band gap (E_g) was calculated by the intercept of the tangent to the plot of $\alpha h\upsilon^r$ vs $h\upsilon$ (Fig. 5b), where α is the absorption constant, h represents the Plank's constant, υ denotes the frequency of incident photons. For materials like CN and the binary composite 10PTCN, the value of r is taken as ½ (Kumaresan et al., 2020), and for PT, the value of r is 2 (Xie et al., 2022). The energy band gap (E_g) was estimated to be 2.69 eV for CN, 2.52 eV for PT which is well supported by previous literatures (Alhaddad et al., 2021; Xu et al., 2021), and 2.56 eV for 10PTCN.

The band edges of CN and PT can be derived based on the equations below (Bai et al., 2023),

$$E_{CB} = \chi - E_e - 0.5E_g \tag{3}$$

$$E_{VB} = E_{CB} + E_g \tag{4}$$

Where, E_e energy of free electron vs. NHE (4.5 eV), E_g is the energy bandgap, and χ is absolute electronegativity of semiconductors and can be obtained by the equation,

$$\chi = \left[\chi(A)^a \chi(B)^b \chi(C)^c\right]^{1/[a+b+c]} \tag{5}$$

Where, a, b and c represent the no. of atoms of A, B and C in the compounds. The values of χ for CN and PT was determined to be 4.73 eV and 5.65 eV, respectively (Bai et al., 2023). Subsequently, the conduction band edge (E_{CB}) and valance band edge (E_{VB}) of CN are –1.12 eV and 1.57 eV vs. NHE, while for PT, the E_{CB} and E_{VB} are –0.11 eV and 2.41 eV respectively. The electronic band arrangements of PT and CN is presented in the Fig. 5c indicating that the conduction band (CB) of both CN and PT are suitable for H_2 production. Further, the charge carrier migration behaviour of the binary heterojunction was studied using PL spectra and presented in Fig. 5d. For the CN sample, the large emission peak emerges at about 460 nm and can be associated with the band to band PL phenomenon, where the light quantum energy is about the same as the CN band gap energy (Ge and Han, 2012). PT does not display these emission characteristics due to its indirect semiconducting features (Xu et al., 2021). The intensity of PL emission peak for 10PTCN is significantly reduced by 57 % as compared to CN, signifies that the reunion of electrons and holes is prevented in the heterojunction.

3.6. Thermal stability analysis

Fig. S2a shows that PT has good thermal stability at high temperatures with no degradation. A typical weight reduction for pure CN occurs

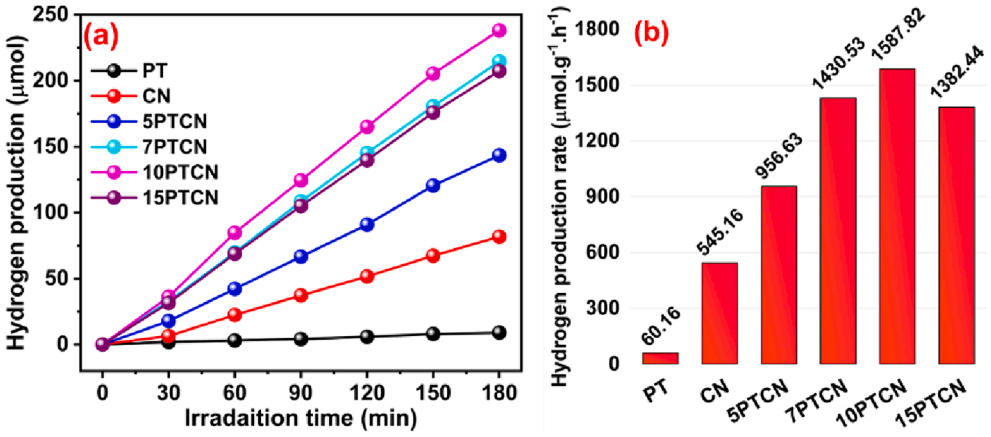

Fig. 6. Photocatalytic performance of PT, CN, and various PTCN photocatalysts, (a) hydrogen production under 300 W Xe irradiation, and (b) bar chart of production rate using various PTCN photocatalysts with a 2.0 wt% Pt co-catalyst.

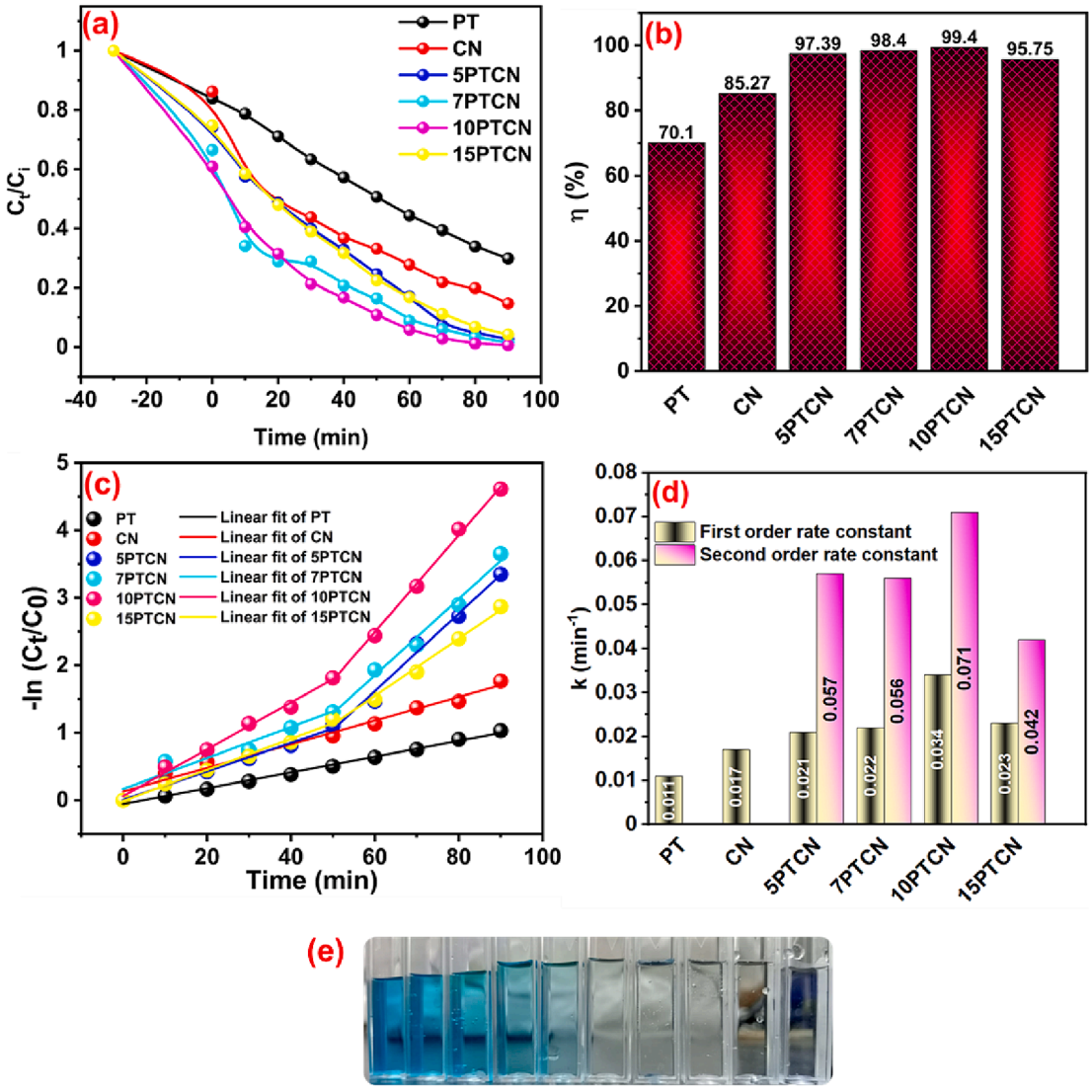

Fig. 7. (a) Photocatalytic MB degradation curves, (b) degradation efficiency, (c) kinetic model, (d) rate constants of various PTCN catalysts, and (e) optical images of MB solution color over 10PTCN sample.

between 490 °C and 610 °C. The decomposition of CN to form graphite and N_2 may be the cause of this weight loss. A small weight reduction (~1%) of PTCN hybrid heterojunction was observed between 50 °C and 100 °C which may be due to the loss of the moisture consumed on the surface of the composites (Oluwole and Olatunji, 2023). The CN and hybrid heterojunction 10PTCN decomposed at 545 °C and 527 °C, respectively (Fig. S2b). However, all the composites are decomposed at a temperature of more than 500 °C which suggests their good thermal stability and can be applicable for photocatalytic applications under 500 °C.

3.7. Photocatalytic activities

3.7.1. Photocatalytic hydrogen production

The activity of simulated sunlight-driven hydrogen evolution rate (HER) was investigated to evaluate the photocatalytic performance of PT, CN, and PTCN hybrid heterojunctions. According to Fig. 6a, PT sample exhibited extremely low HER value. This is a consequence of inadequate charge carrier mobility (Huang et al., 2021). Similarly, the rapid photogenerated charge carrier recombination at the surface of pure CN limits its ability to produce hydrogen. However, all of the PTCN hybrid heterojunction photocatalysts exhibit enhanced hydrogen generation activity after 3 h of irradiation under the same conditions as pure PT and CN. As the amount of PT nanoplates increases in the composite, the HER activity shows an improvement. As shown in Fig. 6b, the HER increases with the addition of PT nanoplates in the heterojunction. The composite 10PTCN shows the maximum HER of 1587.82 μmol.g^{-1}.h^{-1}, which is 26 and 2.9 folds greater than that of PT nanoplates (60.16 μmol.g^{-1}.h^{-1}) and CN (545.16 μmol.g^{-1}.h^{-1}), respectively. As the amount of PT increased beyond 10 % the HER decreased to 1382.44 μmol.g^{-1}.h^{-1} in 15PTCN composite. The higher PT content might agglomerate and block migration of photoinduced electrons and reduce the reaction sites causing a reduction in photocatalytic activity. A high percentage of PT may prevent CN from absorbing light, which will lower the composite's surface reactivity and charge carrier production (Xu et al., 2021). Table S2 summarizes recent works involving CN and PT for photocatalytic hydrogen production. The integration of PT nanoplates with CN nanosheets showed excellent results compared those of previously reported.

3.7.2. Photocatalytic dye degradation

The photocatalytic effectiveness of the photocatalysts was also assessed from dye degradation efficiency. In this study, the photocatalysts were employed to degrade MB dye under 100 W domestic halogen lamp. Fig. 7a shows the MB degradation curves of PT, CN, and PTCN hybrid heterojunctions over time. Similar to the hydrogen production test, the amount of PT affects the degradation activity to a greater extent. As the amount of PT increased, the degradation efficiency increased. Similar to that of HER in Fig. 7b, 10PTCN showed the maximum degradation efficiency up to 99.40 % within 90 min and as the amount of PT increased to 15 % in 15PTCN, the degradation efficiency again decreased. According to previous literatures, the Langmuir-Hinshelwood (L-H) model was employed to investigate the degradation kinetics for synthesized heterogenous photocatalysts in an aqueous medium. Herein, MB solution is diluted to 30 mg.L^{-1}. Hence, for diluted solutions the L-H kinetic model can be simplified into the pseudo first-order kinetic equation as represented in equation (2) (Mondal et al., 2017). Fig. 7c shows the pseudo first-order kinetic model of all the photocatalysts. The pure PT and CN follows a single step pseudo first order reaction for the breakdown of MB, whereas all the binary composites show a two-step trait. A one-step first order expression can fit a large number of reactions as the primary degradation occurs frequently and rapidly. However, the single first-order expression does not fit well for the PTCN heterostructure catalysts. Hence, the kinetic model must consider the intermediate reactions. It should be noted that the semi-log data does not fit the first-order kinetic model for the entire reaction period and fails to produce a single straight line. From previous literatures, it can be observed that complex oxidation reactions tend to be best suited for a consequent series of first order reactions (Shariffuddin et al., 2013). The degradation can be divided into several major steps such as the primary reactant degradation followed by multiple secondary degradation steps leading to the final oxidation to stable products or groups of intermediate products (Mondal et al., 2017). It is found that a two-step series of first-order reactions provides a good model for a breakdown of MB and the intermediates of its azo dye reaction. In Fig. 7c, two linear fits can be observed; one from 0−50 min (k_1) and another from 50−90 min (k_2) associated to the pseudo first order rate constant. According to this two-step reaction process, MB first breaks into azo dye intermediates, which then break into smaller, highly oxidizable intermediate products. These processes proceed very quickly as shown in Fig. 7c revealing only the first linear fit (k_1). The second linear fit (k_2) in the degradation kinetics is produced by these azo dye intermediates, which likely degrade to produce resistant products like Azure A, Azure B, Azure C, and thionine (de Sousa Filho et al., 2020; Mondal et al., 2017; Shariffuddin et al., 2013). The corresponding rate constant for all the photocatalysts is shown in Fig. 7d. 10PTCN shows the maximum first order rate constant for both first and second step showing that 10 wt% loading of PT is optimum for MB photodegradation. The values of rate constants for the photocatalysts are summarized in Table 1. It should be taken into account that in this study, the concentration of MB is very high compared to that of some previously reported photocatalytic MB degradation studies (Table S3). The 10PTCN heterojunction showed a significant degradation efficiency compared to these previous reports. Fig. 7e shows the optical images of the corresponding time-dependent solution color, and Fig. S3a shows the UV–Vis absorption spectra of MB solution at different times.

Table 1
Comparison of photocatalytic MB degradation efficiency for all the photocatalysts.

Photocatalysts	Rate constant k_1 (min^{-1})	Rate constant k_2 (min^{-1})	Degradation efficiency (%)
PT	0.011	–	70.10
CN	0.017	–	85.27
5PTCN	0.021	0.057	97.39
7PTCN	0.022	0.056	98.40
10PTCN	0.034	0.071	99.40
15PTCN	0.022	0.042	95.75

In addition to MB, Photocatalytic degradation of RhB dye solution (10 mg. L^{-1}) was performed (Fig. 8a) for PT, CN, and 10PTCN samples. Similar to previous results, 10PTCN shows improved degradation efficiency of 99.8 % for RhB compared to PT (56.7 %), and CN (85.9 %) under 60 min of irradiation (Fig. 8b). The construction of heterojunction prevented the reunion of photoinduced charge carriers and improved the degradation efficiency. This clearly illustrates the impact of the built-in electric field on the enhanced photocatalytic activity in the 10PTCN catalyst. In contrast to photocatalytic MB degradation, RhB photodegradation showed a single step first order kinetic model as shown in Fig. 8c. The 10PTCN showed the maximum rate constant (Fig. 8d) which is 11.2 and 3.7 times higher than that of PT and CN, respectively. Fig. S3b shows the UV–Vis absorption spectra of RhB solution at different times, while Fig. 8e shows the optical images of the corresponding solution color.

3.7.3. Active-species trapping detection

The results of the scavenger test are presented in Fig. 9. With the addition of EDTA-2Na, MB degradation efficiency has not decreased too much, whereas *t*-BuOH decreased the efficiency from 99.4 % to 76.3 %, The addition of p-BQ and $AgNO_3$ significantly suppressed the MB degradation efficiency to 55.3 % and 50.6 % respectively confirming that $\bullet O_2^-$, e^-, and •OH are the main species accountable for the breakdown of MB. The degradation reaction can be explained using following

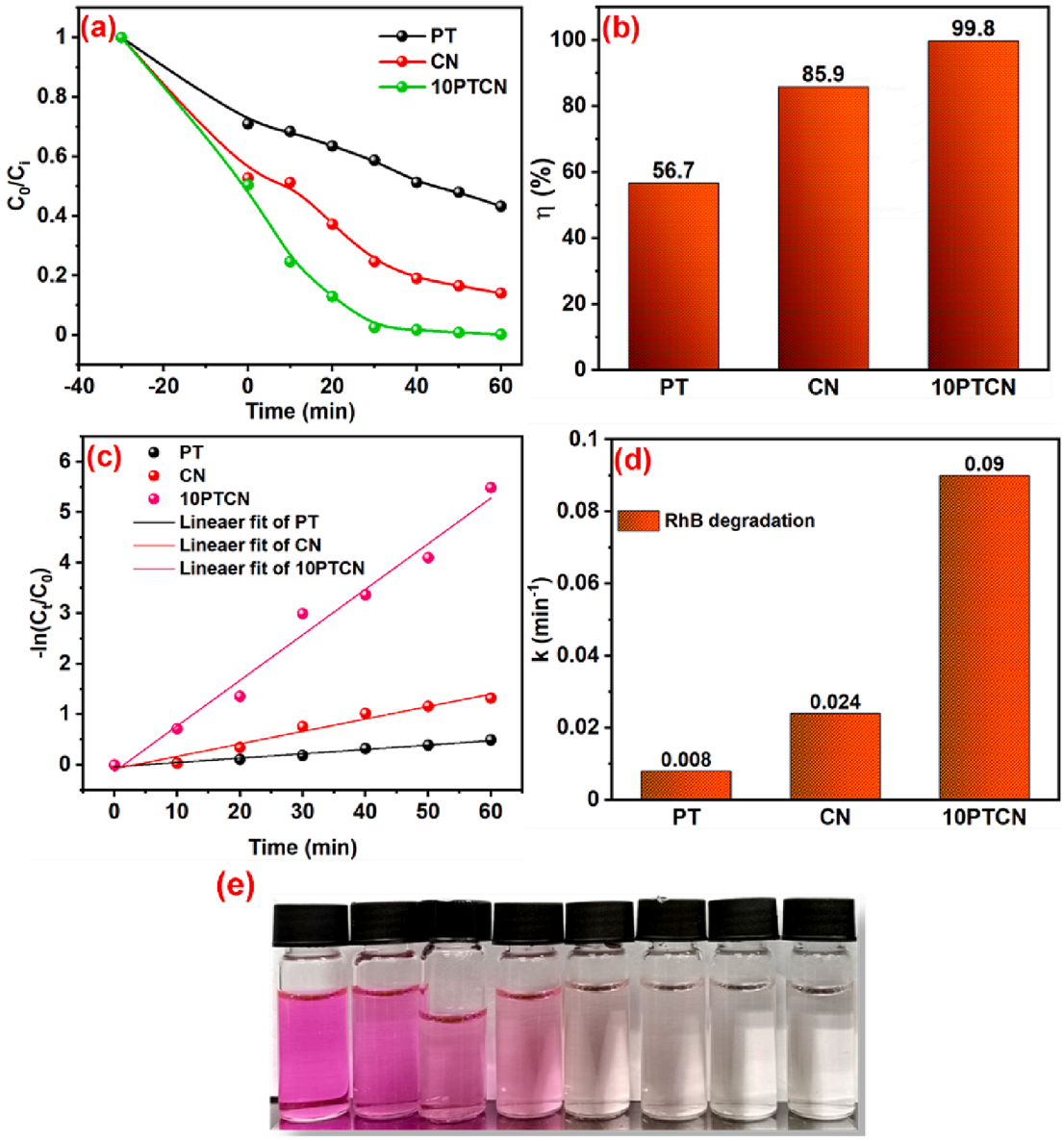

Fig. 8. (a) Photocatalytic RhB degradation curves, (b) degradation efficiency, (c) kinetic curves, (d) rate constants of PT, CN and 10PTCN for RhB degradation, and (e) optical images of corresponding solution color for 10PTCN.

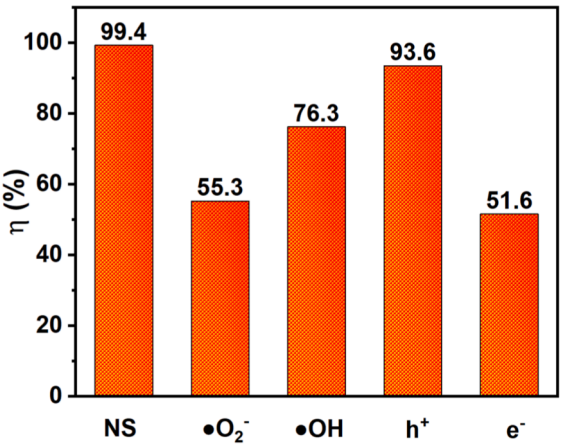

Fig. 9. Active species capture experiments over 10PTCN in presence of various scavengers (here NS means no scavenger).

equations (Hayyan et al., 2016; Zelić et al., 2022),

$$\text{Photocatalysts} + \text{photons} \rightarrow h^+ + e^- \quad (6)$$

$$e^- + O_2 \rightarrow \bullet O_2^- \quad (7)$$

$$H_2O_2 + h^+ \rightarrow \bullet O_2^- + 2H^+ \quad (8)$$

$$H_2O_2 + e^- \rightarrow \bullet OH + OH^- \quad (9)$$

$$\bullet OH + H_2O_2 \rightarrow \bullet HO_2 + H_2O \quad (10)$$

$$\bullet HO_2 \rightarrow \bullet O_2^- + H^+ \quad (11)$$

$$(e^- + \bullet O_2^- + \bullet OH + MB) \rightarrow \text{degradation products} \quad (12)$$

3.7.4. Photocatalytic mechanism analysis

Considering the above outcomes, a possible mechanism is suggested to comprehend the photocatalytic mechanism of PTCN composites. If we consider a type II mechanism, the electrons from CB of CN will transfer

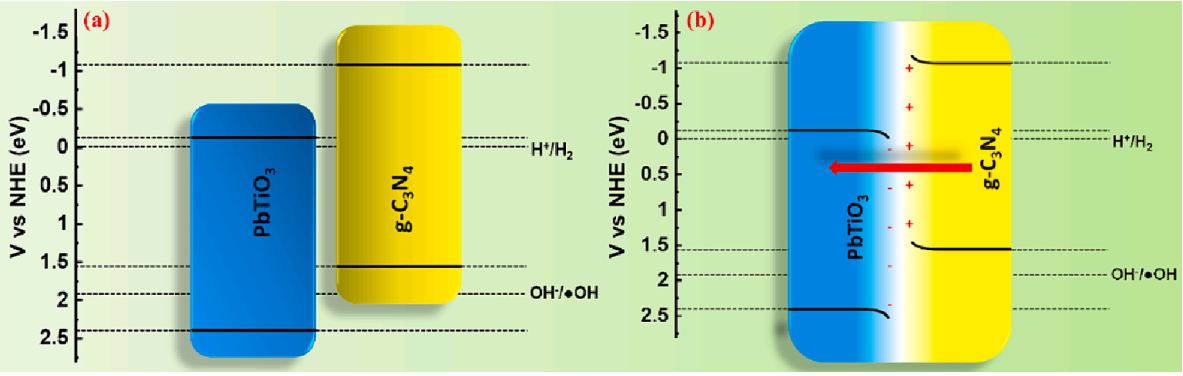

Scheme 2. The schematic representation of heterojunction band alignment (a) before and (b) after contact.

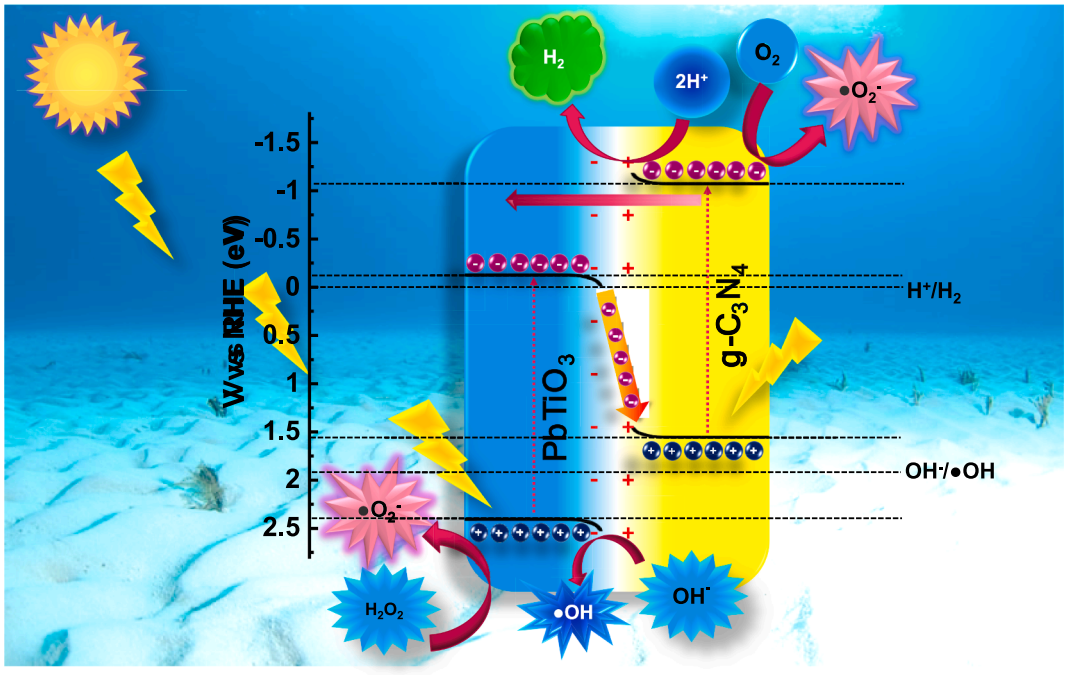

Scheme 3. Schematic representation of photocatalytic S-scheme charge transfer mechanism for 10PTCN under simulated solar irradiation.

to the CB of PT and while the holes from VB of PT would move to the VB of CN. According to the ROS test (Fig. 9), $\bullet O_2^-$, e^- and •OH are the major species accountable for the MB degradation. But the photogenerated electrons in the CB of PT (– 0.11 eV) are more positive than the redox potential of $\bullet O_2^-$ ($O_2/\bullet O_2^-$ = – 0.33 eV). Similarly, the potential of photogenerated holes in the VB of CN (1.57 eV) is more negative than the reduction potential of •OH ($OH^-/\bullet OH$ = +1.99 eV). This confirms that the type II mechanism can't produce $\bullet O_2^-$ and •OH and is invalid here. It can be assumed that 10PTCN is associated to the S-scheme heterojunction because the composite retains both the high oxidation nature of h^+ in PT and the high reduction nature of e^- in CN (Alam et al., 2023; Huang et al., 2022). Before coming in contact (Scheme 2a), the PT and CN have different fermi levels owing to their band structure. After the formation of heterojunction, PT nanoplates and CN nanosheets will come in close contact (Scheme 2b); the electrons from CB of CN will flow towards PT in order to have the same fermi level causing the distortion of CB and VB (Gong et al., 2023). Previously, the XPS analysis (Fig. 3c and d) also confirmed that the electrons migrate from CN to PT. Due to this loss of electrons, the band edges of CN would turn upward and the band edges of PT would bend downward correspondingly forming an internal electric field at the interface between CN and PT.

Upon exposure to solar irradiation (Scheme 3), the photogenerated electrons will jump to conduction bands (CB) in both CN and PT. Owing to the path of band bending, inbuilt electric field, and coulombic interaction, it is tough for electrons to move from CB of CN to the CB PT and h^+ to migrate from VB of PT to the VB CN (Deng et al., 2021). Nevertheless, the excited electrons transfer from CB of PT to recombine with h^+ in the VB of CN along the band bending direction, resulting in a successful segregation of photogenerated charge carriers. As a result, the electrons in CB of CN and h^+ in the CB of PT are preserved to take part in the photocatalytic reaction. This S-scheme heterojunction effectively consumes relatively useless photogenerated electrons (from the CB of PT) and holes (from the VB of CN), but utilizes photogenerated electrons (from the CB of CN) and holes (from the VB of PT), contrary to type-II heterojunctions in which both electrons and holes move towards a more negative potential. Here, methanol is reduced by holes on VB of PT, which acts as a sacrificial agent, and the accumulated electrons on CB of CN combined with H^+, which produces hydrogen.

3.7.5. *Comparative measurement and stability*

The long-term reliability and reuse capability of the photocatalyst are essential from an economic perspective. Cycle stability tests on

10PTCN were performed for both the photocatalytic hydrogen production and the catalytic degradation of MB (Fig. S4a and b). However, the recycling test for hydrogen production demonstrated a slightly reduced catalytic behavior. The hole scavenger solution's consumption and the Pt particles' separation from the catalyst surface following the first cycle may be to blame for this efficiency decline (El-Gendy et al., 2023). Additionally, there is a noticeable alteration in the structure and morphology of 10PTCN after the photocatalytic MB degradation recycle test, as shown by XRD patterns (Fig. S4c) and TEM images (Fig. S4d).

4. Conclusions

In summary, PT nanoplates were synthesized through an efficient hydrothermal method and incorporated with CN via an ultrasonic-assisted hydrothermal method. The XPS and PL results showed the formation of an excellent interface between PT nanoplates and CN. The UV-DRS results showed that the photocatalysts could be utilized under visible light for photocatalytic activities (hydrogen production and dye degradation). The BET results showed the improved surface area of the 10PTCN photocatalyst which demonstrated the excellent photocatalytic HER of 1587.82 μmol. $g^{-1}.h^{-1}$, and degrades 99.40 % of MB dye (30 mg. L^{-1}) and 99.80 % of RhB dye (10 mg.L^{-1}) in 90 and 60 min, respectively. The active species trapping investigation showed that e^- and $\bullet O_2^-$ are the major species for photocatalytic MB degradation. The hybrid heterojunction displayed an S-scheme charge transfer mechanism. This study provides an insightful discussion on the concept of using ferroelectricity to develop next-generation photocatalysts that may be utilized for both environmental remediation and green energy production.

CRediT authorship contribution statement

Rashmiranjan Patra: Writing – original draft, Visualization, Software, Methodology, Investigation, Formal analysis, Data curation, Conceptualization. **Pradeep Kumar Panda:** Writing – review & editing, Writing – original draft, Visualization, Validation, Supervision, Software, Project administration, Methodology, Investigation, Funding acquisition, Formal analysis, Data curation, Conceptualization. **Ting-Han Lin:** Visualization, Methodology, Investigation. **Ming-Chung Wu:** Validation, Methodology, Investigation. **Po-Chih Yang:** Writing – review & editing, Writing – original draft, Visualization, Validation, Supervision, Software, Resources, Project administration, Methodology, Funding acquisition, Formal analysis, Data curation, Conceptualization.

Declaration of competing interest

The authors declare that they have no known competing financial interests or personal relationships that could have appeared to influence the work reported in this paper.

Data availability

No data was used for the research described in the article.

Acknowledgements

This work was supported by the National Science and Technology Council (NSTC), Taiwan, under grant numbers NSTC 111-2221-E-155-003-MY2 and NSTC 112-2811-E-155-002-MY2.

Appendix A. Supplementary data

Supplementary data to this article can be found online at https://doi.org/10.1016/j.ces.2024.120133.

References

Adhikari, S.P., Hood, Z.D., Wang, H., Peng, R., Krall, A., Li, H., Chen, V.W., More, K.L., Wu, Z., Geyer, S., Lachgar, A., 2017. Enhanced visible light photocatalytic water reduction from a g-C_3N_4/$SrTa_2O_6$ heterojunction. Appl. Catal. B 217, 448–458.

Alam, U., Pandey, A., Verma, N., 2023. An anthraquinone-integrated S-scheme-based $NiTiO_3$-g-C_3N_4 composite with enhanced hydrogen production activity. Int. J. Hydrog. Energy 48, 2532–2541.

Alhaddad, M., Shawky, A., Zaki, Z.I., 2021. Reduced graphene oxide-supported $PbTiO_3$ nanospheres: Improved ceramic photocatalyst toward enriched photooxidation of thiophene by visible light. Mol. Catal. 499, 111301.

Bai, L., Huang, H., Yu, S., Zhang, D., Huang, H., Zhang, Y., 2022. Role of transition metal oxides in g-C_3N_4-based heterojunctions for photocatalysis and supercapacitors. J. Energy Chem. 64, 214–235.

Bai, J., Xiang, J., Chen, C., Guo, C., 2023. Piezoelectric-effect-enhanced photocatalytic performance in Cr/Nb modified $Bi_4Ti_3O_{12}$/g-C_3N_4 Z-scheme system. Chem. Eng. J. 456, 141095.

Bao, J., Jiang, X., Huang, L., Quan, W., Zhang, C., Wang, Y., Wang, H., Zeng, Y., Zhang, W., Ma, Y., Yu, S., Hu, X., Tian, H., 2022. Molybdenum disulfide loading on a Z-scheme graphitic carbon nitride and lanthanum nickelate heterojunction for enhanced photocatalysis: Interfacial charge transfer and mechanistic insights. J. Colloid Interface Sci. 611, 684–694.

Chao, C., Ren, Z., Zhu, Y., Xiao, Z., Liu, Z., Xu, G., Mai, J., Li, X., Shen, G., Han, G., 2012. Self-templated synthesis of single-crystal and single-domain ferroelectric nanoplates. Angew. Chem. Int. Ed. 51, 9283–9287.

Chen, F., Huang, H., Guo, L., Zhang, Y., Ma, T., 2019. The role of polarization in photocatalysis. Angew. Chem. Int. Ed. 58, 10061–10073.

Chen, L., Ren, J.-T., Yuan, Z.-Y., 2023. Enabling internal electric fields to enhance energy and environmental catalysis. Adv. Energy Mater. 13, 2203720.

Dash, P., Panda, P.K., Su, C., Lin, Y.-C., Sakthivel, R., Chen, S.-L., Chung, R.-J., 2024. Near-infrared-driven upconversion nanoparticles with photocatalysts through water-splitting towards cancer treatment. J. Mater. Chem. B. https://doi.org/10.1039/D3TB01066J.

de Sousa Filho, I.A., Arana, L.R., Doungmo, G., Grisolia, C.K., Terrashke, H., Weber, I.T., 2020. $SrSnO_3$/g-C_3N_4 and sunlight: Photocatalytic activity and toxicity of degradation byproducts. J. Environ. Chem. Eng. 8, 103633.

Deng, H., Fei, X., Yang, Y., Fan, J., Yu, J., Cheng, B., Zhang, L., 2021. S-scheme heterojunction based on p-type $ZnMn_2O_4$ and n-type ZnO with improved photocatalytic CO_2 reduction activity. Chem. Eng. J. 409, 127377.

El-Gendy, R.A., El-Bery, H.M., Farrag, M., Fouad, D.M., 2023. Metal chalcogenides (CuS or MoS_2)-modified TiO_2 as highly efficient bifunctional photocatalyst nanocomposites for green H_2 generation and dye degradation. Sci. Rep. 13, 7994.

Elmahgary, M.G., Mahran, A.M., Ganoub, M., Abdellatif, S.O., 2023. Optical investigation and computational modelling of $BaTiO_3$ for optoelectronic devices applications. Sci. Rep. 13, 4761.

Feng, Y., Xu, M., Liu, H., Li, W., Li, H., Bian, Z., 2020. Charge separation and interfacial selectivity induced by synergistic effect of ferroelectricity and piezoelectricity on $PbTiO_3$ monocrystalline nanoplates. Nano Energy 73, 104768.

Ge, L., Han, C., 2012. Synthesis of MWNTs/g-C_3N_4 composite photocatalysts with efficient visible light photocatalytic hydrogen evolution activity. Appl. Catal. B 117–118, 268–274.

Gong, S., Zhang, W., Liang, Z., Zhang, Y., Gan, T., Hu, H., Huang, Z., 2023. Construction of a $BaTiO_3$/tubular g-C_3N_4 dual piezoelectric photocatalyst with enhanced carrier separation for efficient degradation of tetracycline. Chem. Eng. J. 461, 141947.

Hassan, Q., Sameen, A.Z., Salman, H.M., Jaszczur, M., Al-Jiboory, A.K., 2023. Hydrogen energy future: Advancements in storage technologies and implications for sustainability. J. Energy Storage 72, 108404.

Hayyan, M., Hashim, M.A., AlNashef, I.M., 2016. Superoxide ion: Generation and chemical implications. Chem. Rev. 116, 3029–3085.

Hisatomi, T., Domen, K., 2019. Reaction systems for solar hydrogen production via water splitting with particulate semiconductor photocatalysts. Nat. Catal. 2, 387–399.

Hisatomi, T., Kubota, J., Domen, K., 2014. Recent advances in semiconductors for photocatalytic and photoelectrochemical water splitting. Chem. Soc. Rev. 43, 7520–7535.

Hu, C., Liu, Z.-T., Yang, P.-C., Ding, Y.-X., Lin, K.-Y.-A., Nguyen, B.-S., 2021. Self-assembly L-cysteine based 2D g-C_3N_4 nanoflakes for light-dependent degradation of rhodamine B and tetracycline through photocatalysis. J. Taiwan Inst. Chem. Eng. 123, 219–227.

Huang, X., Lei, R., Yuan, J., Gao, F., Jiang, C., Feng, W., Zhuang, J., Liu, P., 2021. Insight into the piezo-photo coupling effect of $PbTiO_3$/CdS composites for piezo-photocatalytic hydrogen production. Appl. Catal. B 282, 119586.

Huang, H., Liu, X., Li, F., He, Q., Ji, H., Yu, C., 2022. In situ construction of a 2D $CoTiO_3$/g-C_3N_4 photocatalyst with an S-scheme heterojunction and its excellent performance for CO_2 reduction. Sustain. Energy Fuels 6, 4903–4915.

Ji, X., Yuan, X., Wu, J., Yu, L., Guo, H., Wang, H., Zhang, H., Yu, D., Zhao, Y., 2017. Tuning the photocatalytic activity of graphitic carbon nitride by plasma-based surface modification. ACS Appl. Mater. Interfaces 9, 24616–24624.

Kooshki, H., Sobhani-Nasab, A., Eghbali-Arani, M., Ahmadi, F., Ameri, V., Rahimi-Nasrabadi, M., 2019. Eco-friendly synthesis of $PbTiO_3$ nanoparticles and $PbTiO_3$/carbon quantum dots binary nano-hybrids for enhanced photocatalytic performance under visible light. Sep. Purif. Technol. 211, 873–881.

Kuang, Q., Yang, S., 2013. Template synthesis of single-crystal-like porous $SrTiO_3$ nanocube assemblies and their enhanced photocatalytic hydrogen evolution. ACS Appl. Mater. Interfaces 5, 3683–3690.

Kumaresan, N., Sinthiya, M.M.A., Sarathbavan, M., Ramamurthi, K., Sethuraman, K., Babu, R.R., 2020. Synergetic effect of g-C_3N_4/ZnO binary nanocomposites

heterojunction on improving charge carrier separation through 2D/1D nanostructures for effective photocatalytic activity under the sunlight irradiation. Sep. Purif. Technol. 244, 116356.
Li, R., Li, C., 2017. Chapter One - Photocatalytic Water Splitting on Semiconductor-Based Photocatalysts. In: Song, C. (Ed.), Advances in Catalysis. Academic Press, pp. 1–57.
Li, Y., Li, J., Yang, W., Wang, X., 2020. Implementation of ferroelectric materials in photocatalytic and photoelectrochemical water splitting. Nanoscale Horizons 5, 1174–1187.
Li, T., Tsubaki, N., Jin, Z., 2024. S-scheme heterojunction in photocatalytic hydrogen production. J. Mater. Sci. Technol. 169, 82–104.
Li, Y., Xia, Z., Yang, Q., Wang, L., Xing, Y., 2022. Review on g-C_3N_4-based S-scheme heterojunction photocatalysts. J. Mater. Sci. Technol. 125, 128–144.
Liu, L., Huang, H., 2022. Ferroelectrics in photocatalysis. Chem. Eur. J. 28, e202103975.
Liu, G., Ma, L., Yin, L.-C., Wan, G., Zhu, H., Zhen, C., Yang, Y., Liang, Y., Tan, J., Cheng, H.-M., 2018. Selective chemical epitaxial growth of TiO_2 islands on ferroelectric $PbTiO_3$ crystals to boost photocatalytic activity. Joule 2, 1095–1107.
Liu, Z., Yao, S., Zhang, A., Li, Y., Fu, Y., Zhou, Q., 2023. Intramolecular built-in electric field enhanced polymerized nitrogen-carbon homojunction π*-electron delocalization enrichment promotes photocatalytic uranium (VI) reduction. Appl. Catal. B 338, 123023.
Liu, Y., Ye, S., Xie, H., Zhu, J., Shi, Q., Ta, N., Chen, R., Gao, Y., An, H., Nie, W., Jing, H., Fan, F., Li, C., 2020. Internal-field-enhanced charge separation in a single-domain ferroelectric $PbTiO_3$ photocatalyst. Adv. Mater. 32, 1906513.
Lu, J., Gu, S., Li, H., Wang, Y., Guo, M., Zhou, G., 2023. Review on multi-dimensional assembled S-scheme heterojunction photocatalysts. J. Mater. Sci. Technol. 160, 214–239.
Lv, T., Li, J., Arif, N., Qi, L., Lu, J., Ye, Z., Zeng, Y.-J., 2022. Polarization and external-field enhanced photocatalysis. Matter 5, 2685–2721.
Megía, P.J., Vizcaíno, A.J., Calles, J.A., Carrero, A., 2021. Hydrogen production technologies: From fossil fuels toward renewable sources. A mini review. Energy Fuels 35, 16403–16415.
Meng, A., Cheng, B., Tan, H., Fan, J., Su, C., Yu, J., 2021. TiO_2/polydopamine S-scheme heterojunction photocatalyst with enhanced CO_2-reduction selectivity. Appl. Catal. B 289, 120039.
Mondal, S., De Anda Reyes, M.E., Pal, U., 2017. Plasmon induced enhanced photocatalytic activity of gold loaded hydroxyapatite nanoparticles for methylene blue degradation under visible light. RSC Adv. 7, 8633–8645.
Nasir, M.S., Yang, G., Ayub, I., Wang, S., Wang, L., Wang, X., Yan, W., Peng, S., Ramakarishna, S., 2019. Recent development in graphitic carbon nitride based photocatalysis for hydrogen generation. Appl. Catal. B 257, 117855.
Oluwole, A.O., Olatunji, O.S., 2023. Synthesis and characterization of binary bismuth tungstate-graphitic carbon nitride (BWO/g-C3N4) heterojunction nanocomposites for efficient photodegradation of ibuprofen in aqueous media. J. Water Process Eng. 54, 104045.
Ong, W.-J., Tan, L.-L., Ng, Y.H., Yong, S.-T., Chai, S.-P., 2016. Graphitic carbon nitride (g-C_3N_4)-based photocatalysts for artificial photosynthesis and environmental remediation: Are we a step closer to achieving sustainability? Chem. Rev. 116, 7159–7329.
Osman, A.I., Mehta, N., Elgarahy, A.M., Hefny, M., Al-Hinai, A., Al-Muhtaseb, A.a.H., Rooney, D.W., 2022. Hydrogen production, storage, utilisation and environmental impacts: A review. Environ. Chem. Lett. 20, 153–188.
Paramanika, L., Reddy, H., Sultana, S., Parida, K., 2018. Architechture of Biperovskite-based $LaCrO_3$/$PbTiO_3$ p-n heterojunction with a strong interface for enhanced charge Anti-recombination process and visible light-induced photocatalytic reactions. Inorg. Chem. 57, 15133–15148.
Patra, R., Dash, P., Panda, P.K., Yang, P.-C., 2023a. A breakthrough in photocatalytic wastewater treatment: The incredible potential of g-C_3N_4/titanate perovskite-based nanocomposites. Nanomaterials 13, 2173.
Patra, R., Yang, P.-C., Shu, D.-Y., Hsieh, C.-T., 2023b. Hydrothermal synthesis and ionic sensing properties of graphitic carbon nitride quantum dots. J. Taiwan Inst. Chem. Eng. 150, 105031.
Qin, Y., Xiao, K., Sun, S., Wang, Y., Kang, C., 2023. Fabrication of a novel pyramidal 3D MoS_2/2D $PbTiO_3$ nanocomposites and the efficient photocatalytic removal of organic pollutants: Effects of the $PbTiO_3$ internal electric field and S-scheme heterojunction formation. Appl. Surf. Sci. 616, 156431.
Şen, Z., 2004. Solar energy in progress and future research trends. Prog. Energy Combust. Sci. 30, 367–416.
Shariffuddin, J.H., Jones, M.I., Patterson, D.A., 2013. Greener photocatalysts: Hydroxyapatite derived from waste mussel shells for the photocatalytic degradation of a model azo dye wastewater. Chem. Eng. Res. Des. 91, 1693–1704.
Thommes, M., Kaneko, K., Neimark, A.V., Olivier, J.P., Rodriguez-Reinoso, F., Rouquerol, J., Sing, K.S.W., 2015. Physisorption of gases, with special reference to the evaluation of surface area and pore size distribution (IUPAC Technical Report). Pure Appl. Chem. 87, 1051–1069.
Wang, S., Du, X., Yao, C., Cai, Y., Ma, H., Jiang, B., Ma, J., 2023. S-scheme heterojunction/Schottky junction tandem synergistic effect promotes visible-light-driven catalytic activity. Nano Res. 16, 2152–2162.
Wang, C., Fu, M., Cao, J., Wu, X., Hu, X., Dong, F., 2020. $BaWO_4$/ g-C_3N_4 heterostructure with excellent bifunctional photocatalytic performance. Chem. Eng. J. 385, 123833.
Xie, Z., Shi, J., Tang, X., Wang, Y., Yuan, G., Liu, J.-M., 2022. Piezotronic effect boosted photocatalytic performance of NiO@$PbTiO_3$ p-n heterojunction. Ceram. Int. 48, 16707–16714.
Xing, Z., Ju, Z., Zhao, Y., Wan, J., Zhu, Y., Qiang, Y., Qian, Y., 2016. One-pot hydrothermal synthesis of Nitrogen-doped graphene as high-performance anode materials for lithium ion batteries. Sci. Rep. 6, 26146.
Xu, Q., Ma, D., Yang, S., Tian, Z., Cheng, B., Fan, J., 2019. Novel g-C_3N_4/g-C_3N_4 S-scheme isotype heterojunction for improved photocatalytic hydrogen generation. Appl. Surf. Sci. 495, 143555.
Xu, T., Niu, P., Wang, S., Li, L., 2021. High visible light photocatalytic activities obtained by integrating g-C_3N_4 with ferroelectric $PbTiO_3$. J. Mater. Sci. Technol. 74, 128–135.
Xu, Q., Wageh, S., Al-Ghamdi, A.A., Li, X., 2022. Design principle of S-scheme heterojunction photocatalyst. J. Mater. Sci. Technol. 124, 171–173.
Zelić, I.E., Povijač, K., Gilja, V., Tomašić, V., Gomzi, Z., 2022. Photocatalytic degradation of acetamiprid in a rotating photoreactor - Determination of reactive species. Catal. Com. 169, 106474.
Zhang, Z., Yates Jr., J.T., 2012. Band bending in semiconductors: Chemical and physical consequences at surfaces and interfaces. Chem. Rev. 112, 5520–5551.
Zhang, L., Zhang, J., Yu, H., Yu, J., 2022. Emerging S-scheme photocatalyst. Adv. Mater. 34, 2107668.
Zhu, P., Luo, D., Duan, M., Feng, L., Zhang, S., Liu, M., 2022. Based on a dual Z-scheme heterojunction and magnetically separable $CoFe_2O_4$/g-C_3N_4/$Bi_4Ti_3O_{12}$ flower-like composite for efficient visible-light photocatalytic degradation of organic pollutants. J. Alloys Compd. 911, 164907.